Multifractal analysis of the pore- and solid-phases in binary two-dimensional images of natural porous structures

Annette Dathe , Ana M. Tarquis , Edith Perrier

Abstract

We use multifractal analysis (MFA) to investigate how the Rényi dimensions of the solid mass and the pore space in porous structures are related to each other. To our knowledge, there is no investigation about the relationship of Rényi or generalized dimensions of two phases of the same structure.

Images of three different natural porous structures covering three orders of magnitude were investigated: a microscopic soil structure, a soil void system visible without magnification and a mineral dendrite. Image size was always 1024×1024 pixels and box sizes were chosen as powers of 2. MFA was carried out according to the method of moments, i.e., the probability distribution was estimated for moments ranging from $-10 < q < 10$ and the Rényi dimensions were calculated from the log/log slope of the probability distribution for the respective moments over box sizes. A meaningful interval of box sizes was determined by estimating the characteristic length of the pore space and taking the next higher power of 2 value as the smallest box size, whereas the greatest box size was determined by optimizing the coefficients of determination of the log/log fits for all q. The optimized box size range spans from 32 to 1024 pixels for all images. Good generalized dimension (Dq) spectra were obtained for this box size range, which are capable of characterizing heterogeneous spatial porous structure. They are alike for all images and phases which the exception of the solid mass of the soil void system, which shows a rather flat D_q behavior. A closer examination reveals that similar patterns of structure gain similar spectra of generalized dimensions. The capacity dimension for $q=0$ is close to the Euclidian dimension 2 for all investigated images and phases.

Keywords: Multifractal analysis; Generalized dimensions; Soil structure; Pore space; Solid mass

1. Introduction

Fractal and multifractal concepts have been increasingly applied in various fields of science for describing complexity and self-similarity in nature. Multifractal formalisms involve decomposing self-similar measures into intertwined fractal sets, which are each characterized by their singularity strength and fractal dimension. This type of analysis began to be applied to soil science by Folorunso et al. (1994) to study the soil resistance at different scales in a transect. Later it was used for the analysis of particle size distributions (Grout et al., 1998;

Posadas et al., 2001), volume size distribution of soil aggregates (Martin and Montero, 2002) and pore size distributions (Caniego et al., 2003). Recently, Posadas et al. (2003) applied a multifractal analysis on images of porous media based on previous work done on images of rock pore systems (Muller and McCauley, 1992; Muller et al., 1995; Muller, 1996). The authors compared the multifractal spectrum of binary images with a shape factor determined for the pores and thus distinguished different soil groups with distinguished soil structures.

Reviewing the literature reveals that obtaining a reliable value of the generalized dimension is not an easy calculation to do (Tarquis et al., 2003). Vicsek (1990) proposed practical methods to compute the generalized dimension. He assumed the box size to be much greater than the smallest elementary cell in the system and much smaller than the system size. The main difficulty in using the multifractal formalism lies in the choice of a suited scaling range. In order to describe the important properties of the associated measure to the calculated spectrum several studies only use the generalized dimensions (D_q) for the cases $q=0$, $q=1$ and $q=2$ which can be clearly related to physical properties of the system. For example, several authors have related D_1 to the permeability of sedimentary rocks (Muller and McCauley, 1992; Muller et al., 1995; Muller, 1996). D_2, the correlation dimension, describes the probability of finding pixel pairs representing object in a box or circle of specific size as a function of their distance. Merits and limitations of the multifractal analysis have been discussed by Aharony (1990), Beghdadi et al. (1993), and Andraud et al. (1994). In the same way, Chhabra et al. (1989) pointed out the risks in the estimation of the Hausdorff dimension and cited different sources of errors in some physical cases. The difficulties arising in practice are due to the fact that the relevant quantities used in the multifractal concept are estimated asymptotically and in image analysis these estimations are coarse and limited by the finite resolution of the image (Ahammer et al., 2003) and the measure build on it, as the number of pixels representing object in a box (Buczhowski et al., 1998). In other words, the theoretical limit (when the box-size tends to zero) cannot be reached in practice.

The present work is an extension of results obtained on monofractals by Dathe and Thullner (2005), where mass fractal dimensions were measured for the solid mass and the pore space of porous media. The authors used the pore-solid fractal (PSF) model of Perrier et al. (1999) to obtain a relation between both mass fractal dimensions. It turned out that the phase with the higher percentage of image coverage always gets the higher fractal dimension, with the porosity acting as a weighing factor.

2. Theory: the concept of multifractals

The measurement of multifractals is mainly the measurement of a statistic distribution which is why the results yield useful information even if the underlying structure does not show a self-similar or self-affine behavior (Plotnick et al., 1996). For a monofractal object, the number N of features of a certain size ε varies as

$$N(\varepsilon) \propto \varepsilon^{-D_0}, \tag{1}$$

where the fractal dimension D_0

$$D_0 = \lim_{\varepsilon \to 0} \frac{\log N(\varepsilon)}{\log \frac{1}{\varepsilon}} \tag{2}$$

can be measured by counting the number N of boxes needed to cover the object under investigation for increasing box sizes ε and estimating the slope of a log–log plot. For multifractal measurements, a probability distribution is measured, i.e., the probability in the i^{th} box is

$$p_i(\varepsilon) = \varepsilon^{\alpha_i}, \tag{3}$$

where α_i is the Lipschitz–Hölder exponent characterizing density in the ith box (Halsey et al., 1986). The number of boxes $N(\alpha)$ where the probability has values in the interval $[\alpha, \alpha+d\alpha]$ is found to scale as (Halsey et al., 1986; Chhabra and Jensen, 1989)

$$N(\alpha) \propto \varepsilon^{-f(\alpha)}. \tag{4}$$

In practice, using the box counting method, for every box i the probability of "containing object", also called the partition function, is obtained for different moments q which can vary from $-\infty$ to $+\infty$.

$$X(q, \varepsilon) = \sum_{i=1}^{n(\varepsilon)} p_i^q \tag{5}$$

A log–log plot of the quantity $X(q,\varepsilon)$ over ε for different q yields

$$X(q, \varepsilon) \propto \varepsilon^{-\tau(q)} \tag{6a}$$

$$\text{or } \tau(q) = \lim_{\varepsilon \to 0} \frac{\log X(q, \varepsilon)}{\log \frac{1}{\varepsilon}} \tag{6b}$$

where $\tau(q)$ is called the qth mass exponent. τ and D_q are related as $\tau(q)=(1-q)D_q$. This characterization of

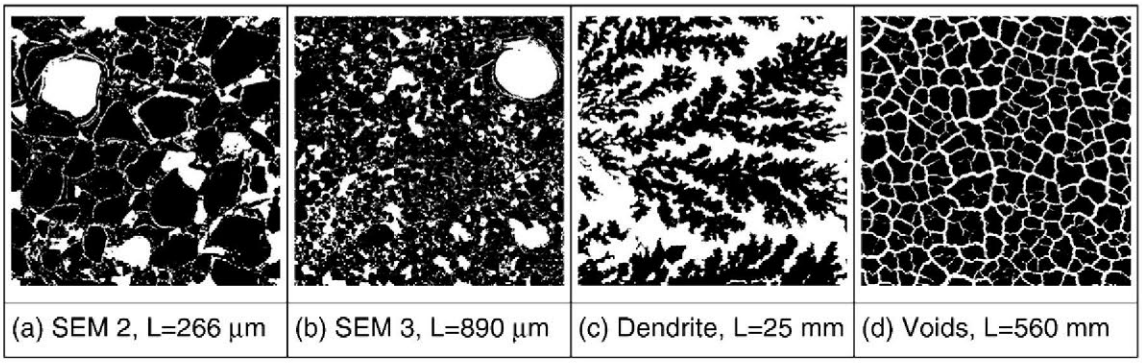

Fig. 1. Images of natural porous structure. (a) and (b) are Scanning Electron Microscope (SEM) images obtained from a soil thin section, (c) shows a mineral dendrite and (d) a top view photo of a soil void system developed in clay. While the original length L of the images is increasing from (a) to (d), their digital size is fixed as 1024×1024 pixels. Solid mass (or object for the dendrite) is presented in black, while pore space (or background, respectively) is represented in white.

multifractal measures is the concept of generalized dimensions D_q, which corresponds to the scaling exponents for the qth moment of the measure. Based on the work of Rényi (1955) they are defined as

$$D_q = \lim_{\varepsilon\to 0}\frac{1}{1-q}\frac{\log\sum_{i=1}^{n(\varepsilon)} p_i^q}{\log\varepsilon} \tag{7}$$

The sum in the numerator of Eq. (7) is dominated by the highest values of p_i for $q>0$, and by the lowest values of p_i for $q<0$.

Moments for $q=1$, 2, ... describe mathematically defined fractal dimensions. They can be found by inserting Eq. (6b) in $D_q=\tau(q)/(1-q)$. For $q=1$ things are more tricky and it can be shown according to Eq. (7) that

$$D_1 = \lim_{\varepsilon\to 0}\frac{\sum_{i=1}^{n(\varepsilon)} p_i\log p_i}{\log\varepsilon} \tag{8}$$

which is the (classical) information dimension: the numerator in Eq. (8) corresponds to the entropy of a probability distribution. This is one of the analogies between multifractals and statistical mechanics. For $q=2$ the correlation dimension D_2 can be obtained as

$$D_2 = \lim_{\varepsilon\to 0}\frac{\log\sum_{i=1}^{n(\varepsilon)} p_i^2}{\log\varepsilon}. \tag{9}$$

It describes the probability of finding pixels belonging to the object within a given distance when starting on a pixel belonging to object. Fractal dimensions for higher moments can be estimated according to Eq. (7). A homogeneous structure is indicated when the D_q are close together, in a monofractal they are equal.

3. Material and methods

3.1. Images of natural porous media

The images SEM 2, SEM 3 and Voids, whose box counting dimension for solid mass, pore space and the interface were measured by Dathe and Thullner (2005), plus the image of a mineral dendrite have been investigated. These are images of three different porous structures: two soil structures occurring on different scales and the mineral dendrite. One of the soil structures (Luvisol developed on Loess, county of Göttingen, Germany) was analyzed on the pore scale (Fig. 1a and b). Images for two different magnifications or resolutions, respectively, were obtained on the µm scale from the polished surface of a soil thin section using a Field Emission Scanning Electron Microscope (SEM). The signal used for detection was composed of 3/4 backscattered and 1/4 secondary electrons at an excitation energy of 18 keV, yielding a depth of focus of about 1 µm. Regions for the investigated images were selected arbitrary from the same thin section for SEM 2 (Fig. 1a), and SEM 3 (Fig. 1b). Dathe et al. (2001) describe in detail the procedure of preparing the samples and obtaining the images. The second soil structure (Pedosol containing about 80% clay, Darling Basin, Australia) represents a soil void system observed on a larger scale (~10 cm, Fig. 1d). Changing water content causes the swelling and shrinking of the clay minerals, yielding the development of voids. The third type of a self-similar pattern, the mineral dendrite (moss agate), is

related to diffusion-limited aggregation (Fig. 1c). Its size lies between the two soil structures.

The SEM images were obtained as 8-bit images (256 gray values for each pixel) by a CCD camera included in the microscopic system. The dendrite was placed on a digital color scanner and scanned directly, yielding a 24-bit-information for each pixel. The image of the soil void system is the top view of the soil surface taken by an analog camera using a film for color prints and digitalized as 24-bit image thereupon. All images were stored with 1024^2 pixels resolution, their original size increases from a side length of 266 μm to 560 mm.

In order to get binary images necessary for the consecutive MFA, the images have to be segmented at a certain threshold. For the SEM images, we took advantage of the clear contrast between the dark pores and the bright soil matrix, assuming a normal distribution of the related gray values for the pores and the matrix, respectively. The scan of the soil void system showed two maxima for the gray values obtained as the average of the three-color channels. The image was segmented at the minimum of the gray value distribution between the maxima for the voids and the matrix. Thresholding the image of the dendrite was more challenging because the gray values of the object and the background were slightly overlapping. Thus the computer scan was segmented taking advantage of the three-color channels by using a higher threshold (corresponding to brighter gray values) for the red channel in combination with lower gray values for the green and blue channels.

3.2. Multifractal analysis

The multifractal analysis has been carried out using a box counting algorithm which estimates the probability of containing mass (pore or solid) for every single box of size 1–1024 pixels in steps 2^k, $1<k<10$. Doing so for images of size 1024×1024 pixels avoids artifacts which can occur when the boxes do not cover the image entirely at the borders. The generalized dimensions are obtained as the slope of the partition function over box size, both taken as logarithm (Eq. (6b)) and the relation $\tau(q)=(1-q)D_q$. This method is known as the method of moments (Evertsz and Mandelbrot, 1992), as D_q is estimated for every moment q. D_1 is simply determined as τ (1).

The computational implementation to calculate the partition function is taking into account that we have a binary image where each pixel is either 0 or 1, see Tarquis et al. (2003) for more details. A crucial step in MFA is to determine the range of box sizes ε and the range of order q over which this analysis is applied (Saucier and Muller, 1998).

Table 1
Characteristic length obtained for the pore space of the respective binary images, using the configuration entropy method

Image	Characteristic length (ε_{min})	Maximum entropy ($H^*(\varepsilon_{min})$)	Minimum box size (pixel)	Maximum box size (pixel)
SEM 2	30	0.748	32	1024
SEM 3	20	0.881	32	1024
Dendrite	30	0.843	32	1024
Voids	26	0.833	32	1024

The minimum box size chosen for the multifractal analysis is the next higher value 2^k.

The minimum box size (ε_{min}) is obtained here based on configuration entropy analysis, which is very easy to implement and has already been used for several types of images (Tarquis et al., 2003, in press). Configuration entropy analysis studies the effect of scale in any measure (a scalar quantity that leads to a positive distribution) defined in a plane. A distribution of the measure is obtained when the measure is estimated for different sizes of areas and every sub-area (Andraud et al., 1994). For small sub-areas (or boxes in an image), the local distributions show a certain behavior that can characterize the spatial pattern of the larger image.

In the work presented, the configuration entropy is estimated for the pore space. The distribution of local porosity in a square lattice image of size L is obtained by subdividing the image into $n(\varepsilon)$ boxes of size ε from $\varepsilon=1$ to $\varepsilon=L/4$; and in every box the number of pixels belonging to the pore space is recorded.

The probability $p_j(\varepsilon)$ of j pixels representing pore space in a box of size ε is defined as:

$$p_j(\varepsilon)=\frac{N_j(\varepsilon)}{n(\varepsilon)}, \tag{10}$$

where $N_j(\varepsilon)$ is the number of boxes with j pixels representing pore space and $n(\varepsilon)$ is the number of boxes of size ε. The configuration entropy H (Andraud et al., 1997)

$$H(\varepsilon)=-\sum_{j=0}^{\varepsilon x\varepsilon} p_j(\varepsilon)\log(p_j(\varepsilon)) \tag{11}$$

expresses the uncertainty of computing the porosity when covering an image with boxes of size ε. This equation is similar to the estimation of the information dimension D_1 (Eq. (8)), where D_1 can be obtained from the slope of the entropy over the logarithm of box sizes.

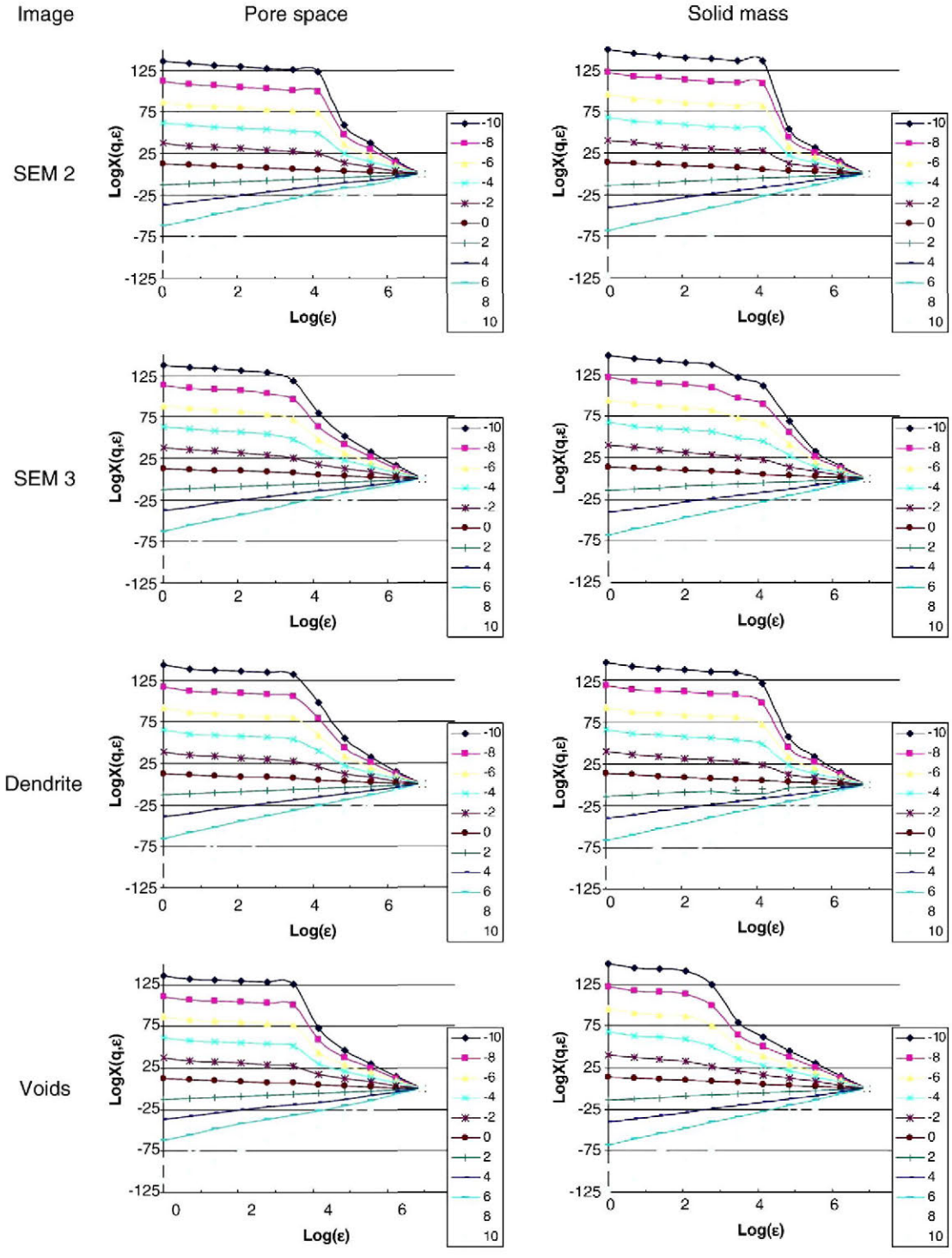

Fig. 2. The partition function of all images for $-10 \le q \le 10$ over box sizes ε ranging from 1 to 1024 pixels. The mass exponent τ is estimated as the slope of the log/log data for (a) the pore space and (b) solid mass for the optimized box size range.

In order to compare entropy values corresponding to different box sizes ε, $H(\varepsilon)$ is normalized to the normalized configuration entropy $H^*(\varepsilon)$:

$$H^*(\varepsilon) = \frac{H(\varepsilon)}{H_{\max}(\varepsilon)} \tag{12}$$

with $H_{\max}(\varepsilon)=\log(\varepsilon^2+1)$.

The curve obtained when plotting the normalized entropy versus ε can be used as a descriptor of the image morphology. In many instances, the curve presents a local maximum $H^*(\varepsilon_{\min})$. The ε value where the maximum is located is called the characteristic length $\varepsilon_{\min}$. The existence or non-existence of $\varepsilon_{\min}$ provides complementary information of spatial arrangements (Rodriguez-Iturbe and D'Odorico, 1998). Results with the characteristic length of the pore space for the images investigated can be found in Table 1.

To select a maximum box size for the MFA the criteria applied is to verify the unweighted coefficients of determination (R^2) for the linear regression of the mass exponent τ to be larger than 0.94, based on the experience of Posadas et al. (2003). We are aware that an R^2 of 0.94 is not a very good fit for the linear regression of log/log data and the number of points used in the regression. However, we are showing the generalized dimensions for $-10<q<10$, as some of the spectra are so similar for positive q that a difference can be observed mainly in the $q<0$ range.

4. Results

Values for the partition function $X(q, \varepsilon)$ have been estimated for the whole available box size range of 1–1024 pixels, in steps of 2^k, $1<k<10$. The partition functions reveal similar shapes for the pore space and solid mass, respectively, for every single image (Fig. 2). For $q>0$, the partition functions of all images investigated show a positive slope with a distinct linear behavior. For $q\leq 0$ the partition functions have a negative slope with a pronounced deviation from linearity for q equal or close to -10. This involves coefficients of determination which are clearly smaller than 1 when estimating the mass exponent τ according to Eq. (6b).

The characteristic length obtained from configuration entropy analysis was taken as a measure for the smallest box size. The next higher value according to 2^k was 32 pixels for all images (Table 1). The maximum box size corresponds to the image size for all images. For the images SEM 2 and the pore space of the image Voids it was not possible to find box ranges where all mass exponents τ for $q<0$ obey the condition $R^2>0.94$. The smallest orders q where the condition is met is $q=-7.5$ for the pore space of SEM 2, $q=-1.5$ for the respective solid mass, and $q=-3.5$ for the pore space of image Voids. No higher R^2 could be achieved by choosing the next smaller box size (512 pixel) as maximum. The range of q for which an $R^2\geq 0.95$ can be found is shown in Table 2. Confirmed by the configuration entropy and the attempt to maximize R^2 values, the box size range is chosen as 32–1024 pixels for all images.

The corresponding generalized dimensions as estimated with Eq. (7) are shown in Fig. 3. They all exhibit pronounced decreasing D_q values with increasing q and reveal a similar behavior for the images SEM 2 and 3 and the Dendrite, as well as the pore space of the image Voids. Generalized dimensions for the solid mass of the image Voids are decreasing as well, but remain within a limited range. Looking at D for $q=-10$ confirms the findings in a quantitative way: the highest values are achieved for image SEM 2 with $D_p(-10)=3.7$ for the pore space and $D_s(-10)=4.0$ for the solid mass. These values are very similar to $D_p(-10)=3.5$ and $D_s(-10)=3.8$ achieved for the image Dendrite. The shape of D_q of image SEM 3 looks smoother for the pore space with $D_p(-10)=3.0$ than for the solid mass $D_s(-10)=3.5$. Image Voids gets $D_p(-10)=3.1$ for the pore space and $D_s(-10)=2.1$ for the solid mass.

Table 2
Results of the generalized dimensions for the first three positive moments q for both, the solid mass and the pore space

Image	Porosity	Phase	$-q$	$+q$	D_0	R^2	D_1	R^2	D_2	R^2	$\Delta(D_0-D_2)$
SEM 2	0.230	Pore	−1.0	10	1.960±0.018	1.000	1.814±0.032	0.999	1.728±0.037	0.998	0.232
		Mass	−0.5	10	1.991±0.003	1.000	1.973±0.005	1.000	1.964±0.006	1.000	0.027
SEM 3	0.264	Pore	−2.0	10	1.999±0.000	1.000	1.913±0.015	1.000	1.838±0.020	1.000	0.161
		Mass	−1.5	10	1.994±0.002	1.000	1.980±0.003	1.000	1.974±0.004	1.000	0.020
Dendrite	0.452	Pore	−1.0	10	1.992±0.005	1.000	1.910±0.019	1.000	1.869±0.022	0.999	0.123
		Mass	−1.0	10	1.982±0.009	1.000	1.929±0.015	1.000	1.906±0.016	1.000	0.076
Voids	0.227	Pore	−1.0	10	1.988±0.007	1.000	1.934±0.029	0.999	1.906±0.038	0.998	0.082
		Mass	−10	10	2.000±0.001	1.000	1.995±0.002	1.000	1.990±0.004	1.000	0.010

Ranges of q where the slope of the partition function exceeds $R^2\geq 0.95$ are given, as well as the standard errors of the slope and the corresponding R^2.

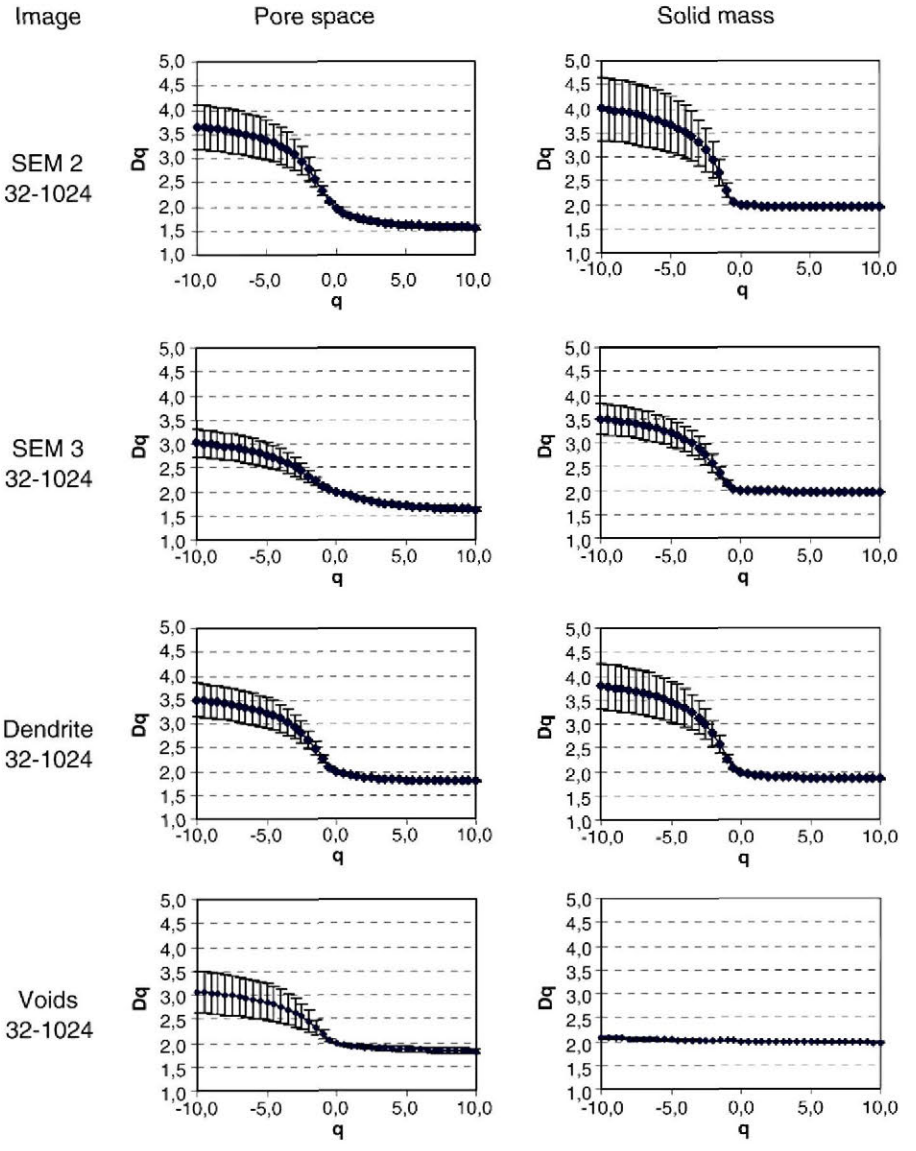

Fig. 3. Generalized dimensions and standard errors of the slope obtained for the optimized box size range of 32–1024 pixels for the images of natural porous structure for (a) the pore space and (b) solid mass.

Generalized dimensions for $q=10$ run from $D_p(10)=1.57$ (SEM 2) to $D_p(10)=1.81$ (Voids) for the pore space and from $D_s(10)=1.85$ (Dendrite) to $D_s(10)=1.97$ (Voids) for the solid mass. The generalized dimensions for $q=10$ are given with two digits because the standard error is 10 to 100 times smaller than the ones for $q=-10$.

Detailed results for D_0, D_1 and D_2 can be found in Table 2, including the corresponding porosities and the q ranges where the mass exponent τ exceeds R^2 values higher than 0.95. Values for D_0, the capacity dimension, run from 1.96 for the pore space of SEM 2 to the Euclidian dimension 2 for the solid mass of the image Voids. The same images and phases show extrema for the information dimension D_1 (1.81 and 1.99) and the correlation dimension D_2 (1.73 and 1.99). The coefficients of determination for D_0, D_1 and D_2 are higher than 0.99 for all images and phases, respectively, and slightly decreasing with increasing q (Table 2).

Main distinction between all images is the difference between D_0 and D_2, $\Delta(D_0-D_2)$. All of the images have a higher difference for the pore space than for the solid mass. The highest difference, $\Delta(D_0-D_2)=0.232$ is found for the pore space of SEM 2, the smallest, $\Delta(D_0-D_2)=$

0.010 for the solid mass of the image Voids. The differences of the generalized dimensions for $q=0$, 1, 2 can also be observed in Fig. 3, where the lower part of the D_q curves ($q \geq 0$) decreases more for the pore phase than for the solid mass.

Standard errors given in Table 2 are the standard errors of the slope obtained with linear regression. They are increasing from D_0 to D_1 and D_2. The smallest standard error which could be found is se=0.00 for D_0 of the pore space of SEM 3, and the highest is 0.04 for D_2 of the pore space of image Voids.

5. Discussion and conclusions

Generalized dimensions D_q have been obtained with the method of moments for different porous media. The graphs of the images SEM 2 and Dendrite look very similar, although their porosities are different with 0.230 and 0.452, respectively. A possible reason is that solid mass and pore space (or object and background of the Dendrite) are distributed in a similar way over the image, revealing areas of non-uniform densities. The graphs of pore space for the images SEM 3 and Voids look similar to each other as well. A closer look at the binarized images (Fig. 1) reveals the pattern of a porous interconnected network which cannot be observed for the other images investigated.

Comparing the capacity dimension D_0 of pore space and solid mass obtained here to a former investigation (Dathe and Thullner, 2005) gives exactly the same values when the same box size range is used. However, for their monofractal analysis the authors used box sizes of 2–32 pixels for the image Voids and 2–64 pixels for the images SEM 2 and SEM 3. Compared to the box size range of 32–1024 pixels applied in the present study, the range of small box sizes leads to clearly distinct values of D_0 for pore space and solid mass. Dathe and Thullner (2005) could demonstrate that the phase with the higher area portion (described by the porosity) always gets the higher fractal dimension. This is not obvious when high box size ranges as in the present study are used. Taking a closer look at Table 2 reveals D_0 values for pore and solid mass which are close together and higher as obtained for the small box size range. D_0 of images SEM 3 and Dendrite even show a higher value for the phase with the lower area portion. Values for D_0 of the images SEM 2 and Dendrite, and for D_1 and D_2 of all images, are higher for the solid mass which is the phase with the higher mass portion.

An explanation why some coefficients of determination (R^2) are rather poor can be found in the graphs of the partition function (Fig. 2). When the slope of log ($X(q, \varepsilon)$) over log (ε) does not yield a straight line for all ε, different generalized dimensions will be obtained for specific ranges of ε. This is why the range of box sizes chosen to determine D_q is crucial regarding the final result, especially for negative moments q. Digital images always have a limited resolution, and only a few pixels can cause great changes in the partition function especially for negative q. Following Evertsz and Mandelbrot (1992), it should be checked carefully whether the slope of $X(q, \varepsilon)$ over ε (the mass exponent τ) yields a straight line before further data processing takes place. The problem is also examined in detail by Saucier and Muller (1993, 1998, 1999) who proposed a systematic method to choose the scaling range for multifractal analysis. The advantage of their method is that a minimum and maximum box size are selected, however, in computational terms the MFA would become more complicated.

More theoretical results and their comparison to measurements are needed to gain knowledge on how to calculate reliable multifractal properties from real data where the range of scale is always finite. A comprehensive tool for performing MFA on digital images for different box size ranges and different bases of the box sizes (e.g., 3^k instead of 2^k) can be found in Perrier et al. (2006-this issue).

Acknowledgements

The funding for one of the authors (AD) of the German Research Foundation under grant number DA 575/1–2, and more recently from Cornell's Biogeochemistry and Biocomplexity Initiative is greatly appreciated. We like to thank Philippe Baveye for providing the digital scan of the mineral dendrite.

References

Ahammer, H., DeVaney, T.T.J., Tritthart, H.A., 2003. How much resolution is enough? Influence of downscaling the pixel resolution of digital images on the generalised dimensions. Physica. D 181 (3–4), 147–156.

Aharony, A., 1990. Multifractals in physics: successes, dangers and challenges. Physica. A 168, 479–489.

Andraud, C., Beghdadi, A., Lafait, J., 1994. Entropic analysis of random morphologies. Physica. A 207, 208–217.

Andraud, C., Beghdadi, A., Haslund, E., Hilfer, R., Lafait, J., Virgin, B., 1997. Local entropy characterization of correlated random microstructures. Physica. A 235, 307–318.

Beghdadi, A., Andraud, C., Lafait, J., Peiro, J., Perreau, M., 1993. Entropic and multifractal analysis of disordered morphologies. Fractals 3, 671–679.

Buczhowski, S., Hildgen, P., Cartilier, L., 1998. Measurements of fractal dimension by box-counting: a critical analysis of data scatter. Physica. A 252, 23–34.

Caniego, F.J., Martin, M.A., San Jose, F., 2003. Rényi dimensions of soil pore size distribution. Geoderma 112 (3–4), 205–216.

Chhabra, A., Jensen, R.V., 1989. Direct determination of the f(alpha) singularity spectrum. Physical Review Letters 62 (12), 1327–1330.

Chhabra, A.B., Menevau, C., Jensen, R.V., Sreenivasan, K.R., 1989. Direct determination of the f(alpha) singularity spectrum and its application to fully developed turbulence. Physical Review. A 40, 5284–5294.

Dathe, A., Thullner, M., 2005. The relationship between fractal properties of solid matrix and pore space in porous media. Geoderma 129 (3–4), 279–290.

Dathe, A., Eins, S., Niemeyer, J., Gerold, G., 2001. The surface fractal dimension of the soil–pore interface as measured by image analysis. Geoderma 103 (1–2), 203–229.

Evertsz, C.J.G., Mandelbrot, B.B., 1992. Multifractal measures. In: Peitgen, H., Juergens, H., Saupe, D. (Eds.), Chaos and Fractals. Springer, Berlin, pp. 921–953.

Folorunso, O.A., Puente, C.E., Rolston, D.E., Pinzón, J.E., 1994. Statistical and fractal evaluation of the spatial characteristics of soil surface strength. Soil Science Society of America Journal 58 (2), 284–294.

Grout, H., Tarquis, A.M., Wiesner, M.R., 1998. Multifractal analysis of particle size distributions in soil. Environmental Science & Technology 32 (9), 1176–1182.

Halsey, T.C., Jensen, M.H., Kadanoff, L.P., Procaccia, I., Shraiman, B.I., 1986. Fractal measures and their singularities—the characterization of strange sets. Physical Review. A 33 (2), 1141–1151.

Martin, M.A., Montero, E., 2002. Laser diffraction and multifractal analysis for the characterization of dry soil volume–size distributions. Soil & Tillage Research 64 (1–2), 113–123.

Muller, J., 1996. Characterization of pore space in chalk by multifractal analysis. Journal of Hydrology 187, 215–222.

Muller, J., McCauley, J.L., 1992. Implication of fractal geometry for fluid flow properties of sedimentary rocks. Transport in Porous Media 8, 133–147.

Muller, J., Huseby, O.K., Saucier, A., 1995. Influence of multifractal scaling of pore geometry on permeabilities of sedimentary rocks. Chaos, Solitons and Fractals 5, 1485–1493.

Perrier, E., Bird, N., Rieu, M., 1999. Generalizing the fractal model of soil structure: the pore-solid fractal approach. Geoderma 88, 137–164.

Perrier, E., Tarquis, A.M., Dathe, A., 2006-this issue. A program for fractal and multifractal analysis of two-dimensional binary images: Computer algorithms versus mathematical theory. Geoderma 134, 284–294. doi:10.1016/j.geoderma.2006.03.023.

Plotnick, R.E., Gardner, R.H., Hargrove, W.W., Prestegaard, K., Perlmutter, M., 1996. Lacunarity analysis: a general technique for the analysis of spatial patterns. Physical Review. E 53 (5), 5461–5468.

Posadas, A.N.D., Gimenez, D., Bittelli, M., Vaz, C.M.P., Flury, M., 2001. Multifractal characterization of soil particle-size distributions. Soil Science Society of America Journal 65 (5), 1361–1367.

Posadas, A.N.D., Gimenez, D., Quiroz, R., Protz, R., 2003. Multifractal characterization of soil pore systems. Soil Science Society of America Journal 67 (5), 1361–1369.

Rényi, A., 1955. On a new axiomatic theory of probability. Acta Mathematica Hungarica VI (3–4), 285–335.

Rodriguez-Iturbe, I., D'Odorico, P., 1998. Configuration entropy of fractal landscapes. Geophysical Letters 25, 1015–1018.

Saucier, A., Muller, J., 1993. Remarks on some properties of multifractals. Physica. A 199, 350–358.

Saucier, A., Muller, J., 1998. Multifractal approach to textural analysis. In: Novak, M.M. (Ed.), Fractals and Beyond, Complexities in the Sciences. World Scientific Publishing Co., London, pp. 161–171.

Saucier, A., Muller, J., 1999. Textural analysis of disordered materials with multifractals. Physica. A 267, 221–238.

Tarquis, A.M., Giménez, D., Saa, A., Díaz, M.C., Gascó, J.M., 2003. Scaling and multiscaling of soil pore systems determined by image analysis. In: Pachepsky, Radcliffe, Selim (Eds.), Scaling Methods in Soil Physics. CRC Press. 434 pages.

Tarquis, A.M., McInnes, K., Keys, J., Saa, A., García, M.R., Díaz, M.C., in press. Multiscaling analysis in a structured clay soil using 2D images. Journal of Hydrology (Available online at http://www.sciencedirect.com).

Vicsek, T., 1990. Mass Multifractal. Physica. A 168, 490–497.